

MULTIWAVELENGTH OBSERVATIONS OF THE POWERFUL GAMMA-RAY QUASAR PKS 1510–089: CLUES ON THE JET COMPOSITION

J. KATAOKA,¹ G. MADEJSKI,² M. SIKORA,³ P. ROMING,⁴ M. M. CHESTER,⁴ D. GRUPE,⁴ Y. TSUBUKU,¹ R. SATO,¹
N. KAWAI,¹ G. TOSTI,⁵ D. IMPIOMBATO,⁵ Y. Y. KOVALEV,^{6,7} Y. A. KOVALEV,⁷ P. G. EDWARDS,⁸
S. J. WAGNER,⁹ R. MODERSKI,³ Ł. STAWARZ,^{2,10} T. TAKAHASHI,¹¹ AND S. WATANABE¹¹

Received 2007 May 25; accepted 2007 September 5

ABSTRACT

We present the results from a multiwavelength campaign conducted in 2006 August of the powerful γ -ray quasar PKS 1510–089 ($z = 0.361$). This campaign commenced with a deep *Suzaku* observation lasting 3 days for a total exposure time of 120 ks and continued with *Swift* monitoring over 18 days. Besides *Swift* observations, the campaign included ground-based optical and radio data and yielded a quasi-simultaneous broadband spectrum from 10^9 to 10^{19} Hz. The *Suzaku* observation provided a high signal-to-noise ratio X-ray spectrum, which is well represented by an extremely hard power law with a photon index of $\Gamma \simeq 1.2$, augmented by a soft component apparent below 1 keV, which is well described by a blackbody model with a temperature of $kT \simeq 0.2$ keV. Monitoring by *Suzaku* revealed temporal variability that differs between the low- and high-energy bands, again suggesting the presence of a second, variable component in addition to the primary power-law emission. We model the broadband spectrum, assuming that the high-energy spectral component results from Comptonization of infrared radiation produced by hot dust located in the surrounding molecular torus. The adopted internal shock scenario implies that the power of the jet is dominated by protons, but with a number of electrons and/or positrons that exceeds the number of protons by a factor of ~ 10 . We also find that inhomogeneities responsible for the shock formation prior to the collision may produce bulk Compton radiation, which can explain the observed soft X-ray excess and possible excess at ~ 18 keV. We note, however, that the bulk Compton interpretation is not unique, as discussed briefly in the text.

Subject headings: galaxies: active — galaxies: jets — quasars: individual (PKS 1510–089) — X-rays: galaxies

Online material: color figures

1. INTRODUCTION

Powerful, highly collimated outflows called jets are commonly observed in a wide variety of astronomical sources; for active galactic nuclei (AGNs; e.g., Urry & Padovani 1995), γ -ray bursts (e.g., Piran 2000), and binaries containing compact stars (e.g., Mirabel & Rodriguez 1999), we have excellent evidence that these outflows move with relativistic speeds. It has been a long-standing mystery, however, as to where and how the relativistic jets are formed and what is their composition. From a theoretical standpoint, the relativistic AGN jets considered here can be launched as outflows dominated by Poynting flux generated in the force-free magnetospheres of black holes or as hydromagnetic winds driven centrifugally from accretion disks (see review by Lovelace

et al. 1999). In either case, strong magnetic fields are involved in driving the outflows, although many (if not most) observations indicate that eventually, *particles* carry the bulk of the jet's energy (Wardle et al. 1998; Sikora & Madejski 2000; Hirotani 2005; Sikora et al. 2005). This apparent discrepancy, however, can be resolved if the jets are indeed initially dominated by the Poynting flux but are efficiently converted into a matter-dominated form at some later stage, most likely prior to the so-called blazar zone (see Sikora et al. 2005 and references therein). Such a blazar zone, the region in which the bulk of the observed nonthermal radiation is produced, is most likely located at $r \simeq 10^3$ – $10^4 r_g$, where $r_g = GM/c^2$ is the gravitational radius (Spada et al. 2000; Kataoka et al. 2001; Tanihata et al. 2003).

Here we adopt a scenario in which a jet is launched near a rapidly rotating black hole, presumably at the innermost portions of the accretion disk (see, e.g., Koide et al. 2000). Such a jet, initially consisting of protons and electrons, is accelerated by large-scale magnetic field stresses, and within $100 r_g$, it can be loaded by electron-positron (e^-e^+) pairs via interactions with the coronal soft γ -ray photons (note that such photons are directly seen in the spectra of Seyfert galaxies; see, e.g., Zdziarski et al. 2000). Hence, it is possible that relativistic jets in quasars (beyond the jet formation zone) may well contain more electron-positron pairs than protons, but are still dynamically dominated by cold protons (Sikora et al. 1997; Sikora & Madejski 2000).

Observations with the EGRET instrument on board the *Compton Gamma Ray Observatory* in the γ -ray band have opened a new window for studying AGN jets, and they have revealed that many radio-bright and variable AGNs are also the brightest extragalactic MeV–GeV γ -ray emitters (see, e.g., Hartman et al. 1999). The properties of the γ -ray emission in those objects, often termed “blazars,” supported earlier inferences based on radio and optical

¹ Department of Physics, Tokyo Institute of Technology, Meguro, Tokyo, 152-8551, Japan.

² Stanford Linear Accelerator Center and Kavli Institute for Particle Astrophysics and Cosmology, Stanford University, Stanford, CA 94305.

³ Nicolaus Copernicus Astronomical Center, Bartycka 18, 00-716, Warsaw, Poland.

⁴ Department of Astronomy and Astrophysics, Pennsylvania State University, University Park, PA 16802.

⁵ Physics Department and Astronomical Observatory, University of Perugia, Perugia, Italy.

⁶ Max-Planck-Institut für Radioastronomie, Auf dem Hügel 69, 53121 Bonn, Germany.

⁷ Astro Space Center of the Lebedev Physical Institute, Profsoyuznaya 84/32, Moscow, 117997, Russia.

⁸ Australia Telescope National Facility, CSIRO, Locked Bag 194, Narrabri NSW 2390, Australia.

⁹ Landessternwarte Heidelberg, Königstuhl, D-69117 Heidelberg, Germany.

¹⁰ Astronomical Observatory of the Jagiellonian University, ul. Orła 171, 30-244 Kraków, Poland.

¹¹ Department of High Energy Astrophysics, ISAS, JAXA, Kanagawa, 229-8510, Japan.

data, and they independently indicated significant Doppler boosting, implying the origin of broadband emission in a compact, relativistic jet pointing close to our line of sight. Generally, the overall spectra of blazar sources [plotted in the $\log(\nu)$ – $\log(\nu F_\nu)$ plane, where F_ν is the observed spectral flux energy density] have two pronounced continuum components, one peaking between the IR and X-rays, and the other in the γ -ray regime (see, e.g., Kubo et al. 1998; Ghisellini et al. 1998). The lower energy component is believed to be produced by the synchrotron radiation of relativistic electrons accelerated within the outflow, while inverse Compton (IC) emission by the same electrons is most likely responsible for the formation of the high-energy γ -ray component. It is widely believed, in addition, that the IC emission from flat-spectrum radio quasars (FSRQs) is dominated by the scattering of soft photons external to the jet (external Compton [EC] process), which are produced by the accretion disk, either directly or indirectly via scattering or reprocessing in the broad-line region (BLR) or a dusty torus (see, e.g., Dermer & Schlickeiser 1993; Sikora et al. 1994). Other sources of seed photons can also contribute to the observed IC component; in particular, the synchrotron photons themselves via the synchrotron self-Compton (SSC) process, which under certain conditions can even dominate the observed high-energy radiation (Sokolov & Marscher 2005). Detailed modeling of broadband blazar emission can provide information about the location of the dissipative regions in blazars, the energy distribution of relativistic electrons and positrons, the magnetic field intensity, and the jet power.

A probe of the low-energy electron and positron content in blazars was proposed by Begelman & Sikora (1987) and has been extensively studied in the literature (Sikora & Madejski 2000; Moderski et al. 2004; Celotti et al. 2007).¹² The γ -ray emission is produced by electrons and positrons accelerated in situ, and thus, before reaching the blazar dissipative site, the electrons and positrons are expected to be cold. If they are transported by a jet with a bulk Lorentz factor of $\Gamma_{\text{jet}} \geq 10$, they upscatter external UV photons to X-ray energies and produce a relatively narrow feature that is expected to be located in the soft- to mid-X-ray band, with the flux level reflecting the amount of cold electrons and the jet velocity. Unfortunately, such an additional bulk Compton (BC) spectral component is difficult to observe because of the presence of strong nonthermal blazar emission, which dilutes any other radiative signatures of the active nucleus. In this context, FSRQs may constitute a possible exception, since their nonthermal X-ray emission is relatively weak when compared to that of other types of blazar sources.

PKS 1510–089 is a nearby ($z = 0.361$) highly polarized quasar (HPQ) detected in the MeV–GeV band by EGRET. It is a highly superluminal jet source, with apparent velocities of $v_{\text{app}} \gtrsim 10c$ observed in multiepoch Very Long Baseline Array (VLBA) observations (Homan et al. 2001; Wardle et al. 2005; Jorstad et al. 2005). Its broadband spectrum is representative of those of other FSRQs. In particular, its radiative output is dominated by the γ -ray inverse Compton component, while its synchrotron emission peaks around IR frequencies below the pronounced UV bump, which is in turn presumably due to the thermal emission from the accretion disk (Malkan & Moore 1986; Pian & Treves 1993). PKS 1510–089 has been extensively studied by X-ray satellites, especially *ROSAT* (Siebert et al. 1996), *ASCA* (Singh et al. 1997), and *Chandra* (Gambill et al. 2003). The observed X-ray spec-

¹² See also Georganopoulos et al. (2005) and Uchiyama et al. (2005) for applications of the bulk Compton constraints on the parameters of AGN jets on large scales.

TABLE 1
2006 *Suzaku* AND *Swift* OBSERVATION LOG OF PKS 1510–089

Start Time (UT)	Stop Time (UT)	Exposure ^a (ks)	Exposure ^b (ks)
<i>Suzaku</i>			
Aug 02 09:31	Aug 05 06:06	119.2	93.4
<i>Swift</i>			
Aug 04 14:09	Aug 04 16:10	2.6	0.10/0.13/0.13/0.27/0.11/0.55
Aug 05 01:10	Aug 05 04:35	2.1	0.09/0.09/0.09/0.17/0.23/0.35
Aug 08 05:07	Aug 08 14:54	2.2	0.07/0.07/0.07/0.14/0.16/0.27
Aug 09 04:49	Aug 09 14:31	1.6	0.07/0.07/0.07/0.14/0.14/0.28
Aug 10 09:47	Aug 10 16:13	0.5	0.05/0.05/0.05/0.12/0.11/0.21
Aug 11 00:15	Aug 11 22:51	4.3	0.14/0.14/0.14/0.29/0.37/0.58
Aug 18 00:57	Aug 18 23:30	3.2	0.13/0.13/0.13/0.27/0.25/0.54
Aug 19 01:02	Aug 19 07:37	2.6	0.11/0.11/0.11/0.22/0.28/0.46
Aug 20 02:46	Aug 20 09:20	2.2	0.09/0.09/0.09/0.18/0.21/0.37
Aug 21 20:32	Aug 22 23:55	3.0	0.13/0.13/0.13/0.25/0.35/0.52

^a *Suzaku*: XIS. *Swift*: XRT.

^b *Suzaku*: HXD. *Swift*: UVOT (*v/b/u/uvw1/uvw2/uvw2*).

trum was very flat in the 2–10 keV band (with a photon index of $\Gamma \simeq 1.3$), but it steepened (to $\Gamma \simeq 1.9$) in the *ROSAT* bandpass (below 2 keV). Recent observations by *BeppoSAX* (Tavecchio et al. 2000) confirmed the presence of a soft X-ray excess below 1 keV. All these findings suggest that PKS 1510–089 may be among the best candidates for detecting the BC bump.

In this paper, we present a detailed analysis of 120 ks of observations of PKS 1510–089 with *Suzaku* in 2006 August as a part of the AO-1 program, in addition to a long *Swift* XRT and UVOT monitoring campaign followed up by ground-based optical and radio telescopes. Thanks to the good photon statistics and the low background of the *Suzaku* and *Swift* data, we successfully obtained the highest quality data on PKS 1510–089 ever reported: over 10 decades in frequency, between 10^9 and 10^{19} Hz. The observation and analysis methods are described in § 2. Detailed spectral studies and temporal analysis are presented in § 3. On the basis of these new findings, in § 4 we discuss the nature of the observed spectral features. Finally, our main conclusions are given in § 5. Throughout this paper, we adopt a luminosity distance of $d_L = 1919$ Mpc for PKS 1510–089 ($z = 0.361$), derived for a modern cosmology with $\Omega_m = 0.27$, $\Omega_\Lambda = 0.73$, and $H_0 = 71$ km s^{−1} Mpc^{−1}.

2. OBSERVATIONS AND DATA REDUCTION

2.1. *Suzaku*

PKS 1510–089 was observed with *Suzaku* (Mitsuda et al. 2007) in 2006 August over approximately 3 days. Table 1 summarizes the start and end times and the exposures of the *Suzaku* observation (sequence 701094010). *Suzaku* carries four sets of X-ray telescopes (Serlemitsos et al. 2007), each with a focal plane X-ray CCD camera (X-ray Imaging Spectrometer [XIS]; Koyama et al. 2007) that is sensitive in the energy range of 0.3–12 keV, together with a non-imaging Hard X-ray Detector (HXD; Takahashi et al. 2007; Kokubun et al. 2007), which covers the 10–600 keV energy band, with Si PIN photodiodes and GSO scintillation detectors. Three of the XIS detectors (XIS 0, XIS 2, and XIS 3) have front-illuminated (FI) CCDs, while the XIS 1 utilizes a back-illuminated (BI) CCD. The merit of the BI CCD is its improved sensitivity in the soft X-ray energy band below 1 keV. PKS 1510–089 was focused on the nominal center position of the XIS detectors.

2.1.1. *XIS Data Reduction*

For the XIS, we analyzed the screened data, reduced via *Suzaku* software version 1.2. The reduction followed the prescriptions described in the *Suzaku* Data Reduction Guide (also known as the ABC Guide)¹³ provided by the *Suzaku* guest observer facility at the NASA Goddard Space Flight Center. The screening was based on the following criteria: (1) only *ASCA* grade 0, 2, 3, 4, and 6 events are accumulated, while hot and flickering pixels were removed from the XIS image using the `cleansis` script; (2) the time interval after the passage of the South Atlantic Anomaly (T_SAA_HXD) is greater than 500 s; and (3) the object is at least 5° and 20° above the rim of the Earth (ELV) during night and day, respectively. In addition, we also select the data with a cutoff rigidity (COR) larger than 6 GV. After this screening, the net exposure for good time intervals is 119.2 ks.

The XIS events were extracted from a circular region with a radius of 4.3' centered on the source peak, whereas the background was accumulated in an annulus with inner and outer radii of 4.9' and 6.3', respectively. We carefully checked that the use of different source and background regions did not affect the analysis results presented in the next sections, within 1 σ uncertainties. The response (RMF) and auxiliary (ARF) files are produced using the analysis tools `xismrfgen` and `xissarmfgen` developed by the *Suzaku* team, which are included in the software package HEASoft version 6.12. We also checked whether our spectral fitting results (see § 3) were consistent with what has been obtained using the “standard” RMF and ARF files provided for science working group members for a point source placed on the nominal CCD position (`ae_xi{0,1,2,3}_20060213.rmf` and `ae_xi{0,1,2,3}_xisnom6_20060615.arf`). This was done after correcting for the degradation of the XIS response using the tool `xisscontamcalc`.

2.1.2. *HXD PIN Data Reduction*

The source spectrum and the light curves were extracted from the cleaned HXD PIN event files (version 1.2). The HXD PIN data are processed with basically the same screening criteria as those for the XIS, except that $\text{ELV} \geq 5^\circ$ through night and day, $\text{T_SAA} \geq 500$ s, and $\text{COR} \geq 8$ GV. The HXD PIN instrumental background spectra were generated from a time-dependent model provided by the HXD instrument team for each observation (see Kokubun et al. [2007] and Fukazawa et al. [2006] for more details; also see Kataoka et al. [2007] concerning the robustness of background subtraction of the HXD PIN using the most recent response and background models). Both the source and background spectra were made with identical good time intervals (GTIs), and the exposure was corrected for detector dead time of 6.3%. We used the response files version `ae_hxd_pinxinom_20060814.rsp`, provided by the HXD instrumental team.

The time-averaged HXD PIN spectrum thus obtained is shown in Figure 1, plotted over the energy range 10–60 keV. HXD PIN data below 12 keV have been ignored to avoid noise contamination near the lower threshold of the PIN diode. In addition, the data above 50 keV are discarded, as a detailed study of noise and background systematics is ongoing above this energy. Figure 1 shows the total (PKS 1510–089 + observed background) spectrum, where the background includes both the instrumental (non-X-ray) background and the contribution from the cosmic X-ray background (CXB; Gruber et al. 1999; see also Frontera et al.

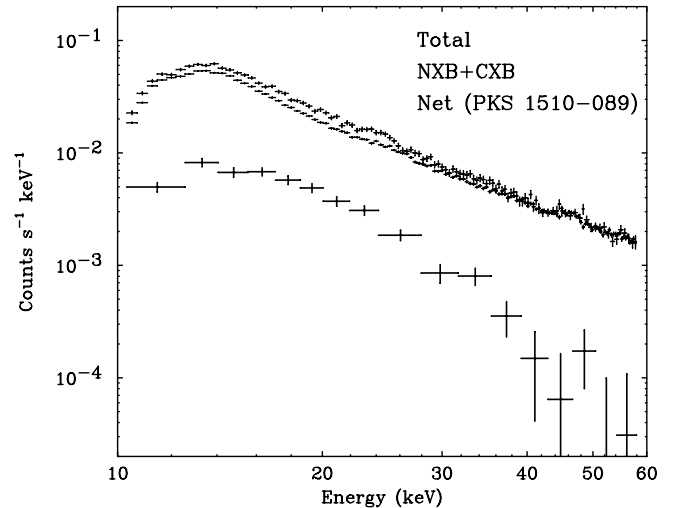


FIG. 1.—Combined HXD PIN spectra for the *Suzaku* observation of PKS 1510–089 over the whole HXD PIN energy bandpass (10–60 keV). *Upper plus signs*, Source plus background spectrum; *middle plus signs*, sum of the non-X-ray background and the CXB; *lower plus signs*, net source spectrum. [See the electronic edition of the *Journal* for a color version of this figure.]

[2007] for updated *BeppoSAX* results). Here the form of the CXB was taken as $9.0 \times 10^{-9} (E/3 \text{ keV})^{-0.29} \exp(-E/40 \text{ keV}) \text{ erg cm}^{-2} \text{ s}^{-1} \text{ sr}^{-1} \text{ keV}^{-1}$, and the observed spectrum was simulated by assuming the PIN detector response to isotropic diffuse emission. When normalized to the field of view of the HXD PIN instrument, the effective flux of the CXB component is expected to be $9.0 \times 10^{-12} \text{ erg cm}^{-2} \text{ s}^{-1}$ in the 12–50 keV band, which is about $\sim 20\%$ of the PKS 1510–089 flux in the same energy bandpass.

If we assumed that the spectral shape determined by the HXD PIN (below 50 keV) would extend to 100 keV, the PKS 1510–089 flux would be $\sim 3.5 \times 10^{-11} \text{ erg cm}^{-2} \text{ s}^{-1}$ (50–100 keV) and could therefore ultimately be detected by the HXD GSO detector. However, this is only a few percent of the GSO detector background, and the study of this level of background systematics is still ongoing by the HXD instrument team. Therefore, in this paper, we do not include the GSO data in the subsequent spectral fits. We also note that after 2006 May 24, bias voltages for 16 out of 64 PIN diodes (in the W0 unit) were reduced from 500 to 400 V to suppress the rapid increase of noise events caused by in-orbit radiation damage.¹⁴ It is thus recommended that a careful comparison of the analysis results including and excluding the W0 unit be made. In this paper, we used all HXD PIN sensors (including W0) because no differences were found between both analyses.

2.2. *Swift*

PKS 1510–089 was observed with *Swift* (Gehrels et al. 2004) 10 times in 2006 August, as a Target of Opportunity (ToO) with a total duration of 24.3 ks. Table 1 summarizes the start and end times and the exposure time of each observation. Note that the *Swift* observations cover more than 18 days, from 2006 August 4 to August 22, and the first two observations are well within the range of the *Suzaku* observation. *Swift* carries three sets of instruments: the Burst Alert Telescope (BAT; 15–150 keV; Barthelmy et al. 2005), the X-ray Telescope (XRT; 0.3–10 keV; Burrows et al. 2005), and the Ultra-Violet/Optical Telescope (UVOT; 170–650 nm; Roming et al. 2005). Hereafter we only analyze the XRT and the UVOT data because the source was not detected in the BAT exposures.

¹³ Available at <http://suzaku.gsfc.nasa.gov/docs/suzaku/analysis/abc>. See also the “seven steps” manuals for the *Suzaku* data analysis, available at <http://www.astro.isas.jaxa.jp/suzaku/analysis>.

¹⁴ See <http://www.astro.isas.jaxa.jp/suzaku/analysis/hxd/v1/hxdresp>.

TABLE 2
OPTICAL OBSERVATION LOG OF PKS 1510–089

Instrument	Filter	Start Time (UT)	Stop Time (UT)	Exposure (s)	Magnitude ^a
REM.....	<i>V</i>	2006 Aug 20 23:14:21	2006 Aug 21 00:00:52	3000	16.88 ± 0.02 ^b
	<i>R</i>	2006 Aug 19 23:13:21	2006 Aug 19 23:59:53	3000	16.10 ± 0.01
	<i>I</i>	2006 Aug 21 00:06:22	2006 Aug 21 00:52:54	3000	16.10 ± 0.01
Heidelberg.....	<i>B</i>	2006 Aug 01 20:25:12	2006 Aug 01 21:19:51	480	16.95 ± 0.08
	<i>R</i>	2006 Aug 01 20:30:22	2006 Aug 01 21:24:23	480	16.15 ± 0.05
	<i>I</i>	2006 Aug 01 20:35:09	2006 Aug 01 21:29:14	360	15.90 ± 0.20

^a Observed magnitude for each observation using specific filters (Galactic extinction not corrected).

^b On August 19, PKS 1510–089 showed a very fast rise ($\Delta m_R \simeq 0.6$) in less than 1 hr.

2.2.1. XRT Data Reduction

The *Swift* XRT data were all taken in Photon Counting mode (PC mode; Hill et al. 2004). The data were reduced by the XRT data analysis task `xrtpipeline` version 0.10.4, which is part of the HEASARC software package, version 6.1. Source photons were selected in a circle with a radius of 47", and background photons were selected in a nearby source-free circle with a radius of 189". Photons were selected from the event file by `xselect` version 2.4. Spectra and light curves were corrected for losses due to dead columns (Abbey et al. 2006). Photons for the spectral analysis with grades 0–12 were selected and rebinned with `grppha` version 3.0.0, with at least 20 photons per bin. The auxiliary response file was created by the XRT task `xrtmkarf` and the standard response file `swxpc0to12_20010101v008.rmf`. All spectra were analyzed in the 0.3–10.0 keV band using XSPEC version 12.3.0 (Arnaud 1996). Due to the low count rate, no correction for pileup was applied.

2.2.2. UVOT Data Reduction

Data from the UVOT and XRT were obtained simultaneously. The UVOT observing mode used one exposure in each of six optical and ultraviolet filters (in order: *uvw2*, *v*, *uvm2*, *uvw1*, *u*, and *b*) per *Swift* pointing (typically 5–15 minutes long). Event data were preserved for *uvm2* and *uvw2*; for the other filters, the data were converted to images on board. Exposures were processed at the *Swift* Data Center. For this analysis, Level 1 event data and Level 2 sky-corrected image data were used. Photometry was performed using the HEASARC FTOOLS tasks `uvotevt1c` for the event data (*uvm2* and *uvw2*) and `uvotsource` for the image data (*v*, *b*, *u*, and *uvw1*) and CALDB version 2006-11-16. Since the source was relatively bright, the source aperture sizes were chosen to correspond to those used to determine the UVOT zero points: 6" for the optical and 12" for the ultraviolet filters. Therefore, no aperture correction was required. A 25" background region was extracted from a blank area of the sky offset from the source. Several blank regions were tried; the choice of background region made only very minor differences to the final results. All event and image data were corrected for coincidence loss. All event data for a given orbit were binned together. A comparison of the event photometry to the ground-processed *uvm2* and *uvw2* images were made; the results were entirely consistent.

2.3. Ground-based Observations

2.3.1. Optical

The photometric optical/IR observations were carried out with two instruments: the Newtonian f/5, 0.4 m Automatic Imaging Telescope (AIT) of the Perugia University Observatory and the

Rapid Eye Mount (REM; see Zerbi et al. 2004), a robotic telescope located at the ESO Cerro La Silla observatory in Chile.¹⁵ The AIT is based on an equatorially mounted 0.4 m Newtonian reflector that has a 0.15 m reflector solidly joined to it. The AIT is a robotic telescope equipped with a 192 × 165 pixel CCD array, thermoelectrically cooled with Peltier elements and using Johnson-Cousins *BVRI* filters for photometry (Tosti et al. 1996).

The REM telescope has a Ritchey-Chrétien configuration with a 60 cm f/2.2 primary and an overall f/8 focal ratio in a fast-moving alt-azimuth mount providing two stable Nasmyth focal stations. At one of the two foci, the telescope simultaneously feeds, by means of a dichroic, two cameras: REMIR for the NIR (see Conconi et al. 2004) and ROSS (see Tosti et al. 2004) for the optical. Both the cameras have a field of view of 10" × 10" and imaging capabilities with the usual NIR (*z'*, *J*, *H*, and *K*) and Johnson-Cousins *VRI* filters. All raw optical CCD frames obtained with the AIT and REM telescopes were corrected for dark, bias, and flat fields. Instrumental magnitudes were obtained via aperture photometry using DAOPHOT (Stetson 1987) and SExtractor (Bertin & Arnouts 1996). Calibration of the source magnitude was obtained by differential photometry with respect to the comparison star sequence reported by Villata et al. (1997) and Raiteri et al. (1998).

In addition, a few optical observations were carried out using a 70 cm telescope of the Landessternwarte in Heidelberg, Germany. Unfortunately, most of the observations were not successful due to bad weather, and we only got data on August 1, just before the *Suzaku* observation started. We obtained *B*, *R*, and *I* photometric measurements (two points each, both consistent with each other within the relative photometric accuracies of 0.01 mag), suggesting no variations on a timescale of an hour within this night. The observation log and resultant magnitudes of PKS 1510–089 during the 2006 August observations are summarized in Table 2.

2.3.2. Radio

The 1–22 GHz instantaneous radio spectrum of PKS 1510–089 was monitored with the 600 m ring radio telescope RATAN-600 (Korolkov & Pariiskii 1979) of the Special Astrophysical Observatory of the Russian Academy of Sciences on 2006 August 9, 10, 11, 22, and 23. Observations were made in the northern sector of the telescope with the secondary reflector of cabin No. 1. The continuum spectrum was measured at six different frequencies (1, 2.3, 4.8, 7.7, 11, and 22 GHz) within 2 minutes in a transit mode. Details on the method of observation, data processing, and calibration are described in Kovalev et al. (1999). Since no significant time variations were found during these observations, the

¹⁵ See <http://www.rem.inaf.it>.

TABLE 3
RADIO OBSERVATION LOG OF PKS 1510–089

Instrument	Frequency (GHz)	Observation Time	Flux Density ^a (Jy)
RATAN	1.0	2006 Aug 9–23	1.88 ± 0.07^b
	2.3	2006 Aug 9–23	2.01 ± 0.05^b
	4.8	2006 Aug 9–23	2.08 ± 0.03^b
	7.7	2006 Aug 9–23	2.09 ± 0.04^b
	11.1	2006 Aug 9–23	2.05 ± 0.21^b
ATCA	21.7	2006 Aug 9–23	1.68 ± 0.08^b
	1.4	2006 Jul 11	1.93 ± 0.11
	2.3	2006 Jul 11	1.83 ± 0.10
	4.8	2006 Jul 11	1.85 ± 0.09
	8.6	2006 Jul 11	1.97 ± 0.10
	1.4	2006 Aug 4	1.85 ± 0.14
	2.4	2006 Aug 4	1.84 ± 0.10
	4.8	2006 Aug 4	2.02 ± 0.10
	8.6	2006 Aug 4	2.12 ± 0.11
	18.5	2006 Aug 4	2.08 ± 0.11
19.5	2006 Aug 4	2.11 ± 0.12	

^a The flux density errors presented do not include the error of the absolute radio flux density scale. See its estimate in Baars et al. (1977) and Ott et al. (1994).

^b RATAN flux densities are averaged over the period 2006 August 9–23.

averaged data of the five independent spectral measurements are provided in Table 3.

PKS 1510–089 was also observed with the Australia Telescope Compact Array (ATCA). ATCA consists of six 22 m diameter paraboloidal antennas (Frater et al. 1992), with five antennas on a 3 km east-west track that has a 214 m north-south spur, and a sixth antenna fixed 3 km to the west of the east-west track. Snapshot observations were made with ATCA on two dates. The first observations were made on 2006 July 11 at 1.4, 2.3, 4.8, and 8.6 GHz while the array was in the 750B configuration, with a maximum baseline of 4.5 km. The second observations were made on 2006 August 4 in the H168 configuration, using the inner five telescopes, with a maximum baseline of 192 m, at frequencies of 18.5 and 19.5 GHz, in addition to the same four frequencies that were used in the first epoch. PKS 1934–638 was used as the primary flux density and bandpass calibrator at both epochs. Data

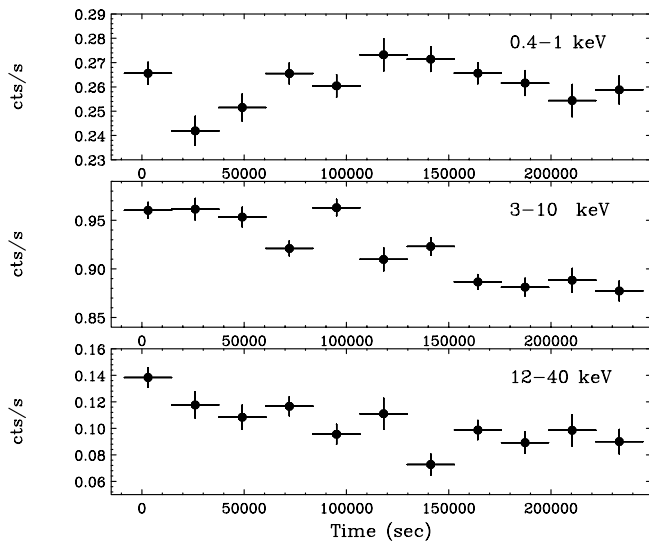


FIG. 2.—Overall variability of PKS 1510–089 observed with *Suzaku* in 2006 August. *Top*, 0.4–1 keV (XIS 0–3 summed); *middle*, 3–10 keV (XIS 0–3 summed); *bottom*, 12–40 keV (HXD PIN W0–3 summed). [See the electronic edition of the *Journal* for a color version of this figure.]

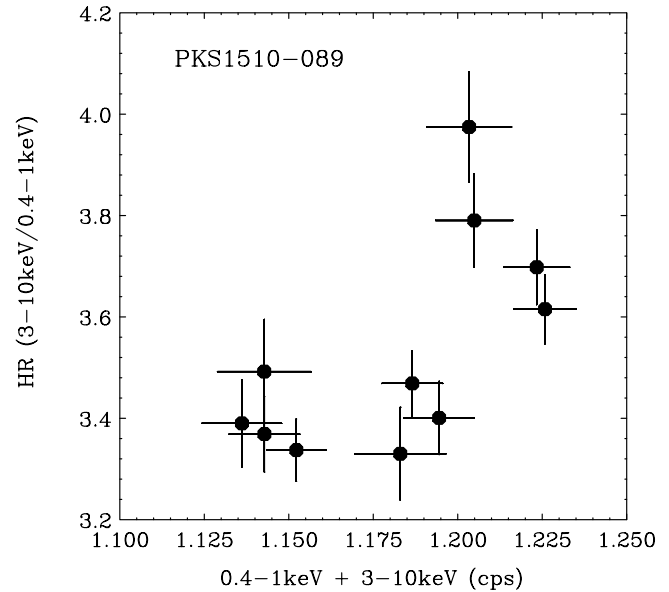


FIG. 3.—Changes in the hardness ratio between 0.4–1 keV and 3–10 keV. The hardness is defined as the 3–10 keV count rate divided by the 0.4–1 keV count rate (XIS 0–3 summed). [See the electronic edition of the *Journal* for a color version of this figure.]

were reduced with MIRIAD, and the flux densities were calculated under the assumption that the source is pointlike, using the task `uvflux` (Sault et al. 1995). The flux densities at both the first and the second epochs are summarized in Table 3. The errors in the flux densities include the intrinsic scatter in the data and a conservative allowance of 5% for systematic variation in the flux density scale (Tingay et al. 2003).

3. RESULTS

3.1. *Suzaku*

During the *Suzaku* observation (August 2–5; Table 1), PKS 1510–089 was in a relatively bright state, with an average net count rate of the four XISs, measured in the 0.4–10 keV range, of 2.388 ± 0.003 counts s^{-1} . For the PIN detector, the net average source count rate in the 12–40 keV band was 0.105 ± 0.003 counts s^{-1} , compared to the PIN background (non-X-ray background) rate of 0.425 counts s^{-1} . Figure 2 shows count rate variations during the *Suzaku* observation. The light curves of the four XISs and the HXD PIN detectors are shown separately in different energy bands: 0.4–1 keV (*top*; XIS), 3–10 keV (*middle*; XIS), and 12–40 keV (*bottom*; HXD PIN). This clearly indicates different variability properties: count rates decreased above 3 keV (*middle and bottom*), while they reached a delayed maximum ~ 1.5 days from the start of the *Suzaku* observation for the 0.4–1 keV band.

Spectral evolution during the observation is best illustrated as a correlation between the source brightness and the hardness ratio. Figure 3 shows the count rate (sum of the 0.4–1.0 keV and 3–10 keV counts) versus the hardness ratio, which is defined as the ratio of the XIS count rates at 3–10 keV to those at 0.4–1.0 keV. This suggests a spectral evolution with the spectrum hardening as the source becomes brighter, although the correlation is rather loose, especially when the source is in the lower state of activity (e.g., when the sum of the 0.4–1 keV and 3–10 keV count rates is less than 1.2 counts s^{-1}). In addition, the hardness parameter is not a linear function of the source brightness, at least for the relatively short timescale of the *Suzaku* observation (i.e., within 3 days). Again, this may suggest that more than just one spectral

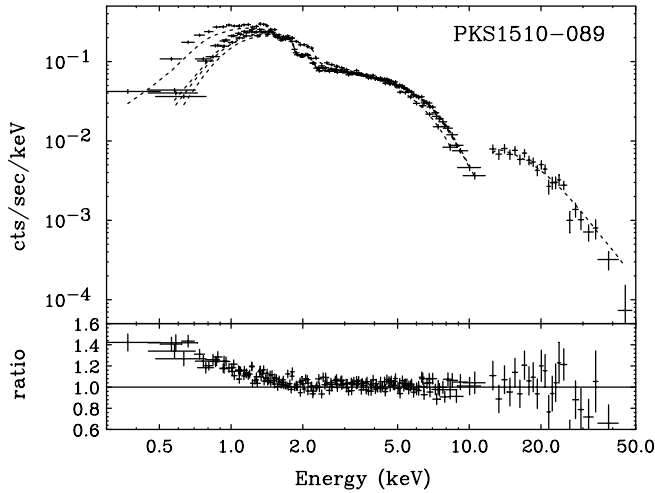


FIG. 4.—Broadband (0.3–50 keV; XIS 0–3 + HXD PIN) *Suzaku* spectrum of PKS 1510–089. The top panel shows the data, plotted against an absorbed power-law model with a photon index of $\Gamma = 1.2$ and a column density of $7.88 \times 10^{20} \text{ cm}^{-2}$, fitted over the 2–50 keV band. The bottom panel shows the data/model ratio residuals to this power-law fit. Deviations due to excess soft emission can be clearly seen. [See the electronic edition of the *Journal* for a color version of this figure.]

component contributes to the observed X-ray emission of PKS 1510–089.

The XIS and HXD PIN background-subtracted spectra were fitted using XSPEC version 11.3.2, including data within the energy range 0.3–50 keV. We binned the XIS spectra to a minimum of 400 counts bin^{-1} to enable the use of the χ^2 minimization statistic. The Galactic absorption toward PKS 1510–089 is taken to be $N_{\text{H}} = 7.88 \times 10^{20} \text{ cm}^{-2}$ (Lockman & Savage 1995). All errors are quoted at the 68.3% (1σ) confidence level for the parameter of interest unless otherwise stated. All the fits in this section are restricted to the energy ranges 0.5–12 keV (XIS 0, XIS 2, and XIS 3: the FI chips), 0.3–9 keV (XIS 1: the BI chip), and 12–50 keV (HXD PIN). In the following analysis, we fixed the relative normalization of the XISs and PIN at 1.13, which is carefully determined from calibration using the Crab Nebula, pointed at the XIS nominal position (Ishida et al. 2006).

Figure 4 shows the spectrum of the four XISs and the HXD PIN, with residuals, plotted against the best-fit power-law (PL) model determined using data between 2 and 50 keV. The residuals of Figure 4 indicate that the spectrum exhibits significant soft excess emission below 2 keV. If we model the overall X-ray spectrum between 0.3 and 50 keV with a simple power-law function modified by the Galactic absorption, we obtain the best-fit photon

index $\Gamma_{\text{high}} = 1.30$, but the fit is statistically unacceptable, with a χ^2/dof of 705/585, where “dof” indicates degrees of freedom (Table 4). To represent the concave shape of the observed X-ray spectrum, we first consider a double power-law function (PL+PL) in which the soft X-ray excess is due to a steep power-law component with a photon index of $\Gamma_{\text{low}} \simeq 2.7$. This provides an acceptable fit, with $\chi^2/\text{dof} = 536/583$, although the wavy structure still remains, especially below 1 keV.

Hence, we considered an alternative fit consisting of a hard power-law function with $\Gamma_{\text{hard}} = 1.23$ and a blackbody (BB) component or a disk blackbody (DB; Mitsuda et al. 1984) feature. Both models give a similarly good representation of the data, with the best $\chi^2/\text{dof} = 515/583$ for the latter (Table 4). The improvement of the χ^2 statistic is significant at more than the 99.9% confidence level when compared to the PL+PL model described above ($\Delta\chi^2 \simeq 20$ for 583 dof). The temperature of the introduced thermal component is fitted as $kT \simeq 0.2 \text{ keV}$. Figure 5 shows an absorption-corrected νF_{ν} spectrum deconvolved with this PL+DB model. The integrated luminosity of this blackbody-type emission is $L_{\text{BB}} \simeq (2.6 \pm 0.2) \times 10^{44} \text{ erg s}^{-1}$.

3.2. *Swift*

The deep *Suzaku* observations of PKS 1510–089 over 3 days (120 ks in total) are well complemented by the *Swift* XRT observation for monitoring the long-term variability of this source on the weeklong scale. In addition, the first two observations made by *Swift* were simultaneous with the *Suzaku* observations (see Table 1) and thus provide an important opportunity for the cross-calibration of results between the two instruments. Since the effective area of the *Swift* XRT is less than 10% of the XIS on board *Suzaku* in the 0.5–10 keV range, detailed spectral modeling is difficult using the *Swift* data alone. Furthermore, the average exposure for the *Swift* segment was only a few kiloseconds, which was much less than the *Suzaku* exposure of 120 ks. We therefore fit the XRT data simply with a power-law function in the energy band 0.3–10 keV, modified by the Galactic absorption.

Figure 6 compares the variations of the X-ray flux and changes in the power-law spectral photon index as a function of time. Here the observation time is measured from the start of the *Suzaku* observation; i.e., 2006 August 2, 09:31 UT. Note the wide range of source variability (about a factor of 2) on a weeklong scale, which was not observed with *Suzaku*. The dashed lines in this figure show the time coverage and the best-fit parameter determined by *Suzaku* (the two dashed lines show the 1σ uncertainty of the *Suzaku* parameters). We confirm that the results obtained with *Suzaku* and *Swift* are perfectly consistent with each other. Figure 7 shows the relation between the 0.5–10 keV flux versus the photon index measured by the *Swift* XRT (the data from

TABLE 4
RESULTS OF THE SPECTRAL FITS TO THE 0.3–50 keV *Suzaku* SPECTRUM WITH DIFFERENT MODELS

Model ^a	N_{H}^{b}	$\Gamma_{\text{high}}^{\text{c}}$	$\Gamma_{\text{low}}^{\text{d}}$	kT^{e}	$F_{0.5-10 \text{ keV}}^{\text{f}}$	$F_{2-10 \text{ keV}}^{\text{f}}$	$F_{10-50 \text{ keV}}^{\text{f}}$	χ^2/dof
PL.....	7.88	1.30 ± 0.01	14.1 ± 0.1	10.8 ± 0.1	33.7 ± 0.4	705/585
PL+PL.....	7.88	1.19 ± 0.02	2.76 ± 0.15	...	14.4 ± 0.1	11.1 ± 0.1	39.7 ± 0.5	536/583
PL+BB.....	7.88	1.24 ± 0.01	...	0.16 ± 0.02	14.2 ± 0.1	11.1 ± 0.1	38.3 ± 0.4	519/583
PL+DB.....	7.88	1.23 ± 0.01	...	0.23 ± 0.02	14.4 ± 0.1	11.1 ± 0.1	38.2 ± 0.4	515/583

^a Spectral fitting models. PL, power-law function; PL+PL, double power-law functions; PL+BB, power law + blackbody model; PL+DB, power law + disk blackbody model.

^b Galactic absorption column density, in units of 10^{20} cm^{-2} .

^c Differential spectral photon index.

^d Differential spectral photon index at the low-energy X-ray band, when fitted with a double power-law function.

^e Temperature at inner disk radius, in units of keV, fitted with disk blackbody model by Mitsuda et al. (1984).

^f Flux, in units of $10^{-12} \text{ erg cm}^{-2} \text{ s}^{-1}$.

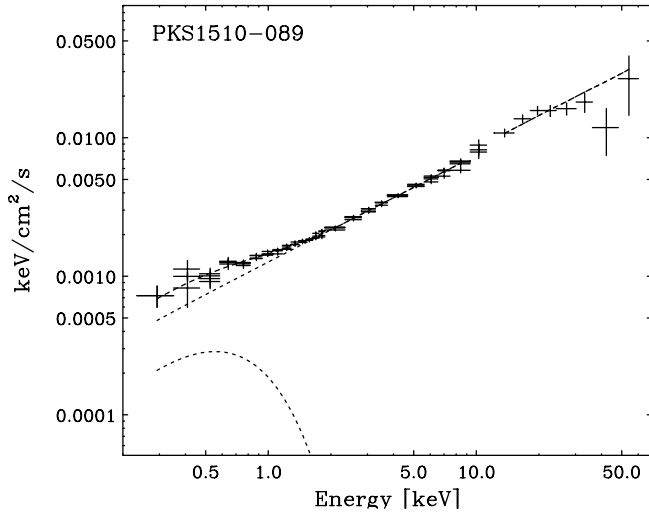


FIG. 5.—Unfolded *Suzaku* spectrum between 0.3 and 50 keV (in νF_ν space), plotted against the best-fit model composed of an absorbed power law ($\Gamma = 1.2$; upper dotted line) plus disk blackbody emission ($kT = 0.2$ keV; lower dotted line). The dashed line shows the sum of the model components. [See the electronic edition of the *Journal* for a color version of this figure.]

August 10 were excluded, as they have large statistical uncertainties due to the short exposure; see Table 1). Clearly the X-ray spectrum becomes harder when the source gets brighter. Such a trend is often observed in high-frequency peaked BL Lac objects (e.g., Kataoka et al. 1999), but it has not previously been observed so clearly in a quasar-hosted blazar such as PKS 1510–089.

Thanks to the excellent sensitivity and wideband coverage of the *Swift* UVOT, even relatively short 1 ks exposures provide the deepest UV-optical measurement ever reported for this source in the literature. To cover as much bandpass as possible, we used all the filters (*v*, *b*, *u*, uvw1, uvm2, and uvw2) for all 10 observations (Table 1). The fluxes in each filter were corrected for Galactic extinction following the procedure described in Cardelli et al. (1989), calculating the Galactic extinction with the values

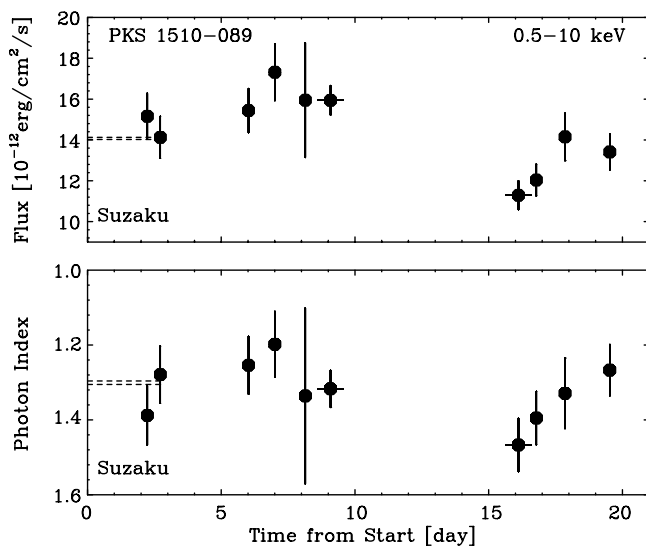


FIG. 6.—Spectral variability of the *Swift* XRT data during the 2006 August campaign. The observation time is measured from the start of the *Suzaku* observation, i.e., 2006 August 2, 09:31:29 UT, and the dashed lines show the best-fit parameters determined by *Suzaku*. *Top*: Changes in the 0.5–10 keV fluxes. Absorption has been corrected. *Bottom*: Changes in the power-law photon index. [See the electronic edition of the *Journal* for a color version of this figure.]

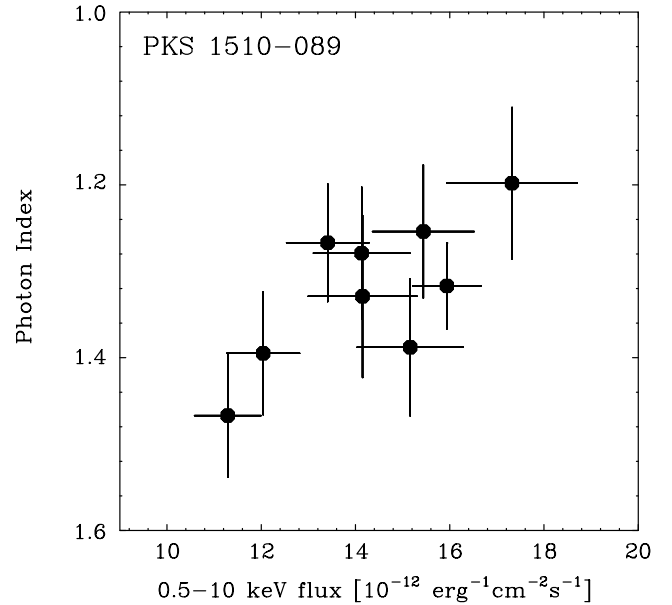


FIG. 7.—Correlation of the 0.5–10 keV flux vs. photon index measured by the *Swift* XRT. Data for the fifth observation has been ignored in this plot simply due to its large uncertainties (see error bars in Fig. 6). [See the electronic edition of the *Journal* for a color version of this figure.]

$R_V = 3.1$ and $E_{B-V} = 0.097$ taken from Schlegel et al. (1998). We note that the expected extinction value is somewhat higher than the one given by Burstein & Heiles (1982; E_{B-V} between 0.06 and 0.09). We generated a list of the amount of extinction that needs to be accounted for in each filter, $A_\lambda = E_{B-V}(aR_V + b)$, where a and b are constants, that is summarized in Table 5. The resulting correction factor to each of the filters were 1.32, 1.45, 1.56, 1.82, 1.91, and 2.09, respectively, for the *v*-, *b*-, *u*-, uvw1-, uvm2-, and uvw2-band filters. The extinction-corrected light curves thus produced are shown in Figure 8. In contrast to the X-ray light curve (Fig. 6), no significant variability was detected throughout the 2006 August campaign.

Finally, Figure 9 shows the combined optical/UV spectrum of PKS 1510–089 taken during the campaign. Circles show the average *Swift* UVOT data, whereas squares and crosses show data taken by the Landessternwarte at Heidelberg and by REM, respectively. Note the excellent agreement between the *Swift* UVOT and other telescopes at optical wavelengths. The overall trend of

TABLE 5
CORRECTION FACTORS FOR THE GALACTIC EXTINCTION
IN UV AND OPTICAL FILTERS

Filter	λ^a (nm)	a^b	b^b	A_λ^b	C_{cor}^c
<i>I</i>	800	0.7816	−0.5707	0.18	1.18
<i>R</i>	650	0.9148	−0.2707	0.25	1.26
<i>v</i>	547	1.0015	0.0126	0.30	1.32
<i>b</i>	439	0.9994	1.0171	0.40	1.45
<i>u</i>	346	0.9226	2.1019	0.48	1.56
uvw1.....	260	0.4346	5.3286	0.65	1.82
uvm2.....	249	0.3494	6.1427	0.70	1.91
uvw2.....	193	−0.0581	8.4402	0.80	2.09

^a Center wavelength for each optical and UV filter.

^b Parameters for calculating Galactic extinction for optical and UV filters, calculated according to the prescription in Cardelli et al. (1989). The Galactic reddening was taken from Schlegel et al. (1998).

^c Correction factor for Galactic extinction.

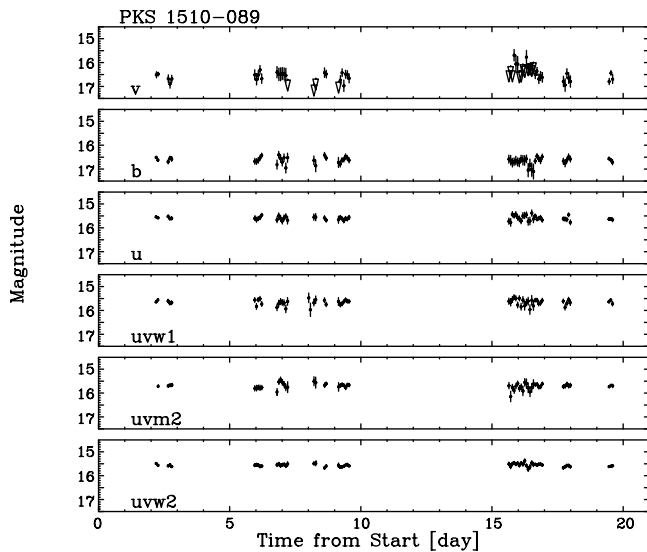


FIG. 8.—Overall variability of the *Swift* UVOT data during the 2006 August campaign. From top to bottom: *v*-, *b*-, *u*-, *uvw1*-, *uvm2*-, and *uvw2*-band data. For more details about the UVOT filters and their wavelength properties, see T. Poole et al. (2008, in preparation) and http://swift.gsfc.nasa.gov/docs/swift/about_swift/uvot_desc.html. [See the electronic edition of the *Journal* for a color version of this figure.]

the optical/UV continuum is that the flux density (F_ν , in units of mJy) decreases with increasing frequency, such that $F_\nu \propto \nu^{-0.57}$. Also, it appears that the spectrum shows an interesting dip or discontinuity around $\nu \sim 10^{14.7}$ and $10^{15.0}$ Hz. No discontinuity is evident in the combined infrared/optical/UV spectral energy distribution and line flux measurements (e.g., Mg II) provided by Malkan & Moore (1986). However, strong line emission present in a single *Swift* UVOT filter can produce an apparent discontinuity. The discrepancy may also be explained by the fact that the observations reported by Malkan & Moore (1986) were obtained over several epochs.

4. DISCUSSION

4.1. Flat X-Ray Continuum and Spectral Evolution

In the previous sections we have presented temporal and spectral analyses of *Suzaku* and *Swift* observations of PKS 1510–089 in 2006 August. The great advantage of using all the *Suzaku* and *Swift* instruments is that we can resolve the spectral evolution on different timescales, from hours (*Suzaku*) to weeks (*Swift*). In particular, our campaign provided the first detection of time variability as short as the day scale in the hard X-ray energy band (12–40 keV). During the *Suzaku* observations, PKS 1510–089 was in a relatively high state with an average flux of $F_{2-10 \text{ keV}} \sim 1.1 \times 10^{-11} \text{ erg cm}^{-2} \text{ s}^{-1}$, which gradually decreased by about 10% over the duration of the observation. Historically, the flux observed with *Suzaku* is more than 2 times higher than that observed with *BeppoSAX* in 1998 ($5.2 \times 10^{-12} \text{ erg cm}^{-2} \text{ s}^{-1}$) or with *ASCA* in 1996 ($8.6 \times 10^{-12} \text{ erg cm}^{-2} \text{ s}^{-1}$). The *Swift* XRT sampled a range of continuum fluxes during the 18 days of the campaign, detecting significant spectral evolution, with the photon index Γ changing from 1.2 to 1.5.

The observed photon index is significantly lower than that of radio-loud quasars ($\langle \Gamma \rangle = 1.66 \pm 0.07$; Lawson et al. 1992; Cappi et al. 1997) or radio-quiet quasars ($\langle \Gamma \rangle = 1.90 \pm 0.11$; Lawson et al. 1992; Williams et al. 1992) and is more similar to the ones observed in high-redshift quasars. For example, in the sample of 16 radio-loud quasars at $z > 2$ considered by Page et al. (2005), four sources have hard spectra with $\Gamma = 1.4$ (see also Tavecchio

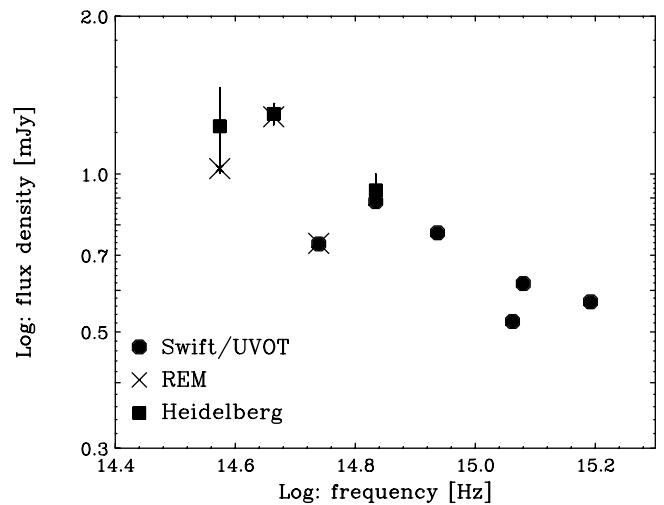


FIG. 9.—Combined optical/UV spectrum of PKS 1510–089 taken during the 2006 August campaign. Data are corrected for Galactic extinction using the relations in Cardelli et al. (1989). Note the perfect consistency between the *Swift* UVOT, REM, and Heidelberg telescopes. [See the electronic edition of the *Journal* for a color version of this figure.]

et al. [2000] for 0836+710 and Sambruna et al. [2006] for the *Swift* blazar J0746+2449, with $\Gamma \simeq 1.3$). Such hard X-ray spectra pose a challenge to the “standard” shock models of particle acceleration, because they imply a very flat electron energy distribution. As long as the X-ray emission is due to the low-energy tail of the EC spectral component, a photon index of $\Gamma = 1.2$ corresponds to an electron energy distribution of $N(\gamma) \propto \gamma^{-1.4}$, where γ is the Lorentz factor of the ultrarelativistic (radiating) electrons.

This may suggest that shocks, if indeed they are responsible for accelerating the jet particles, can produce relativistic electrons with an energy spectrum much harder than the “canonical” power-law distribution, $N(\gamma) \propto \gamma^{-2}$, or that another mechanism energizes the electrons, at least at low energies, $\gamma \leq 10$, that are typically involved in the production of the X-ray emission within the EC model (e.g., Tavecchio et al. 2007). The latter possibility was discussed by Sikora et al. (2002), who assumed a double power-law form of the injected (“freshly accelerated”) electrons, with a break energy of $\gamma_{\text{br}} \sim 10^3$ corresponding to the anticipated threshold of diffusive shock acceleration.¹⁶ Below that energy, the electrons must be accelerated by a different mechanism, e.g., involving instabilities driven by shock-reflected ions (Hoshino et al. 1992) or magnetic reconnection (Romanova & Lovelace 1992).

These “alternative” processes can possibly account for the electron distribution being harder than $\propto \gamma^{-2}$. The X-ray emission of PKS 1510–089 discussed here provides direct constraints on this crucial low-energy population of ultrarelativistic electrons in quasar jets. At the other end of the spectrum of the Compton component, archival EGRET (and, in the future, *GLAST*) observations may be used to constrain the high-energy tail of the accelerated electrons.

In this context, it is interesting to revisit the spectral evolution detected with the *Swift* XRT in PKS 1510–089. In general, the trend established for FSRQs is that only little X-ray variability is observed on short timescales of hours to days. Even on longer timescales, the X-ray variations in FSRQs are usually small, and the X-ray spectral shape is almost constant. The best example for such behavior is 3C 279, where the X-ray slope changed only a little during the historical outburst in 1988, from $\Gamma = 1.70 \pm 0.06$

¹⁶ See, in this context, Stawarz et al. (2007) for the case of particle acceleration at mildly relativistic shocks in large-scale jets.

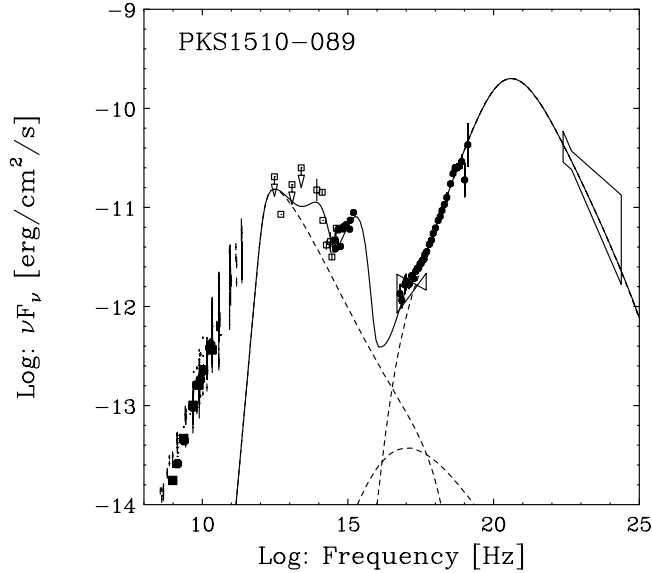


FIG. 10.—Overall SED of PKS 1510–089 constructed with multiband data obtained during this campaign (filled circles); radio (RATAN-600 and ATCA), optical (*Swift* UVOT, REM, and Heidelberg), and X-ray (*Suzaku*). Historical data taken from radio (NED and CATS), IR (*IRAS*; Tanner et al. 1996), optical (NED), soft X-ray (*ROSAT*; Siebert et al. 1996; *left bow tie*), and γ -ray (EGRET; Hartman et al. 1999; *right bow tie*) databases are also plotted as black points. The solid line shows the spectrum calculated using the jet emission model described in the text, as a sum of various emission components [dotted lines, from left to right; synchrotron, SSC, and EC(IR)]. The input parameters for this model are as follows: $\gamma_{\min} = 1$, $\gamma_{\text{br}} = 100$, $\gamma_{\max} = 10^5$, $p = 1.35$, $q = 3.25$, $K_e = 0.9 \times 10^{47} \text{ s}^{-1}$, $\Gamma_{\text{jet}} = 20$, $\theta_{\text{jet}} = 0.05 \text{ rad}$, $\theta_{\text{obs}} = 0.05 \text{ rad}$, $r_{\text{sh}} = 10^{18} \text{ cm}$, $B = 1.3 \text{ G}$, $r_{\text{ext}} = 3.0 \times 10^{18} \text{ cm}$, $L_{\text{ext}} = 3.7 \times 10^{45} \text{ erg s}^{-1}$, and $h\nu_{\text{ext}} = 0.2 \text{ eV}$. See Moderski et al. (2003) for the definition of the input parameters. [See the electronic edition of the *Journal* for a color version of this figure.]

to 1.58 ± 0.03 (Makino et al. 1989). However, exceptions were found recently in several distant quasars. For example, the X-ray spectral slope of RBS 315 changed from $\Gamma = 1.3$ to 1.5 between two observations separated by 3 yr (Tavecchio et al. 2007). Also, the hard X-ray spectrum of 0836+710 softened from $\Gamma \simeq 1.4$ (as measured by *BeppoSAX*; Tavecchio et al. 2000) to $\Gamma \simeq 1.8$ (*Swift* observations; Sambruna et al. 2007).

Such a variability pattern may simply imply that the distribution of ultrarelativistic electrons at low energies changes (although not dramatically) in some sources. Another explanation, however, is that this spectral shape remains roughly constant, but that the amount of contamination from the soft excess emission varies, affecting the spectral fitting parameters at higher energies ($E \geq 2 \text{ keV}$). In fact, we showed that the photon index became a little steeper ($\Delta\Gamma \simeq 0.1$; Table 4) when we fit the spectrum with a simple power-law function. This suggests that the spectral evolution of PKS 1510–089 may be explained by the soft excess emission being more important when the source gets fainter and becoming almost completely “hidden” behind the hard X-ray power law ($\Gamma_{\text{hard}} \simeq 1.2$) when the source gets brighter.

4.2. Modeling the Overall SED

Figure 10 shows the overall spectral energy distribution (SED) of PKS 1510–089 during the 2006 August campaign. Large filled circles represent simultaneous data from the radio (RATAN-600 and ATCA), optical (*Swift* UVOT, REM, and Heidelberg), and X-ray (*Suzaku*) observations. Historical data taken from radio (NED and CATS), FIR (*IRAS*, Tanner et al. 1996), optical (NED), soft X-ray (*ROSAT*; Singh et al. 1997), and γ -ray (EGRET; Hartman et al. 1999) observations are also plotted as black points or bow ties. Figure 10 implies that the synchrotron component of

PKS 1510–089 most likely peaks around 10^{12} – 10^{14} Hz , while the excess at NIR frequencies may be due to the starlight of the host, and the excess at the FIR may be due to dust radiation from the nuclear torus. Meanwhile, our UVOT, REM, and Heidelberg data show “rising” emission in the frequency range between $10^{14.4}$ and $10^{15.2} \text{ Hz}$, with $\nu F_\nu \propto \nu^{0.43}$ (§ 3.2). As already suggested in the literature (e.g., Malkan & Moore 1986; Pian & Treves 1993), this is most likely a manifestation of a strong UV excess (“blue bump”), which is thought to be produced by the accretion disk and/or corona near the central black hole of PKS 1510–089. Apparently, these optical/UV data do not join smoothly with the X-ray–to– γ -ray spectrum, which is due to the nonthermal EC jet radiation. Also note that the X-ray spectrum softens at low energies due to the presence of soft excess emission, as suggested by the detailed spectral fitting in Figures 4 and 5.

To reproduce the overall SED of PKS 1510–089, we applied the numerical model BLAZAR developed in Moderski et al. (2003), updated for the correct treatment of the Klein-Nishina regime (Moderski et al. 2005). The code is based on a model in which the nonthermal flares in blazars are produced in thin shells propagating down a conical jet with relativistic velocities. The production of nonthermal radiation is assumed to be dominated by electrons and positrons that are accelerated directly, rather than being injected by pair cascades. The code traces the time evolution of the synchrotron and IC components, where both the synchrotron and external photons are considered as seed radiation fields contributing to the IC process. We assumed that the electrons are injected by the shock formed at a distance $0.5r_{\text{sh}}$, propagating with a Lorentz factor Γ_{sh} , and decaying at $r = r_{\text{sh}}$, and that the injection function takes the broken power-law form

$$Q_\gamma = K_e \frac{1}{\gamma^p + \gamma_{\text{br}}^{p-q} \gamma^q}, \quad (1)$$

where K_e is the normalization factor, p and q are the spectral indices of the injection function at the low- and high-energy limits, respectively, and γ_{br} is the break energy.

The comoving energy density of the external radiation is approximated via

$$u'_{\text{ext}} = \frac{4}{3} \Gamma_{\text{sh}}^2 \frac{L_{\text{ext}}}{4\pi c r_{\text{ext}}^2} \frac{1}{1 + (r/r_{\text{ext}})^n}, \quad (2)$$

where L_{ext} and r_{ext} are the total luminosity and the scale (spatial extent) of the considered external photon field, respectively, and $n \geq 2$. We investigated radiation fields from both the dusty torus and the BLR and found that Comptonization of the former better reproduces the observed spectrum. Our fit of PKS 1510–089 is shown in Figure 10, and the model parameters are specified in the figure caption and in Table 6 (“Model A”). The presented model is a snapshot at the maximum of the flare, which corresponds roughly to the distance r_{sh} . Note that $r_{\text{sh}} > r_{\text{BLR}}$, but r_{sh} is still much below the radio photospheres, and the observed flat-spectrum radio emission originates from the superposition of more distant, self-absorbed portions of the outflow.

4.3. Energetics and Pair Content

In order to derive the power and pair content of a jet, the dynamics and structure of the shock must be specified. We adopt here the internal shock scenario and assume that shells with relativistic plasma represent regions enclosed between the reverse and forward shock fronts. Such a structure is formed by colliding inhomogeneities propagating down the jet with different Lorentz factors. In this model, the light curves are produced by a sequence

TABLE 6
INPUT PARAMETERS FOR MODELING THE NONTHERMAL EMISSION OF PKS 1510–089

Parameter	Model A	Model B
Minimum electron Lorentz factor, γ_{\min}	1	1
Break electron Lorentz factor, γ_{br}	100	150
Maximum electron Lorentz factor, γ_{\max}	10^5	10^5
Low-energy electron spectral index, p	1.35	1.35
High-energy electron spectral index, q	3.25	3.25
Normalization of the injection function, K_e (s^{-1}).....	0.9×10^{47}	1.7×10^{47}
Bulk Lorentz factor of the emitting plasma, Γ_{jet}	20	20
Jet opening angle, θ_{jet} (rad).....	0.05	0.02
Jet viewing angle, θ_{obs} (rad).....	0.05	0.05
Scale of the emission zone, r_{sh} (cm).....	10^{18}	10^{18}
Jet magnetic field intensity, B (G).....	1.3	0.86
Scale of the dominant external photon field, r_{ext} (cm).....	3.0×10^{18}	3.0×10^{18}
Luminosity of the external photon field, L_{ext} (erg s^{-1}).....	3.7×10^{45}	3.7×10^{45}
Photon energy of the external photon field, $h\nu_{\text{ext}}$ (eV).....	0.2	0.2
Total energy of radiating electrons, E_e (erg).....	1.3×10^{48}	3.1×10^{48}
Comoving electron energy density, u'_e (erg cm^{-3}).....	0.015	0.022
Equipartition magnetic field, B_{eq} (G).....	0.6	2.4
Kinetic luminosity of radiating electrons, L_e (erg s^{-1}).....	1.4×10^{45}	3.3×10^{45}
Type of soft X-ray excess.....	Bulk Compton	SSC

of shocks with a range of locations and lifetimes (Spada et al. 2000). Our fit, presented in Figure 10, shows the radiative output of the shock operating over a distance range of $\Delta r = 0.5 \times 10^{18}$ cm, starting at 0.5×10^{18} cm and decaying at $r_{\text{sh}} = 10^{18}$ cm. The amount of electrons and positrons injected into the shell by the end of the shock operation is

$$N_{e,\text{inj}} = t'_{\text{sh}} \int_{\gamma_{\min}} Q_{\gamma} d\gamma \simeq \frac{\Delta r}{c\Gamma_{\text{sh}}} \frac{K_e}{(p-1)\gamma_{\min}^{p-1}} \simeq 2.9 \times 10^{53}, \quad (3)$$

where $t'_{\text{sh}} = \Delta r / (c\Gamma_{\text{sh}})$ is the lifetime of the shock as measured in the rest frame of the shock (discontinuity surface).

The electrons and positrons are accelerated or injected, resulting in an average energy of $\bar{\gamma}_{\text{inj}} = \int Q_{\gamma} \gamma d\gamma / \int Q_{\gamma} d\gamma \simeq 22$ that follows from the model parameters as given in the caption of Figure 10 and in Table 6. Assuming that this energy is taken from protons, we have a ratio of electrons and positrons to protons of

$$\frac{N_e}{N_p} = \eta_e \frac{m_p(\bar{\gamma}_p - 1)}{m_e \bar{\gamma}_{\text{inj}}}, \quad (4)$$

where η_e is the fraction of the proton thermal energy tapped by the electrons and positrons. The value of $\bar{\gamma}_p - 1$, which actually represents the efficiency of the energy dissipation, depends on the properties and speeds of the colliding inhomogeneities and is largest if they have the same rest densities and masses. In this case, if we assume that $\Gamma_2 > \Gamma_1 \gg 1$,

$$\bar{\gamma}_p - 1 = \frac{(\sqrt{\Gamma_2/\Gamma_1} - 1)^2}{2\sqrt{\Gamma_2/\Gamma_1}}, \quad (5)$$

and $\Gamma_{\text{sh}} = (\Gamma_1 \Gamma_2)^{1/2}$ (Moderski et al. 2004).

We assume hereafter that $\Gamma_1 = 10$ and $\Gamma_2 = 40$, and, using equations (4) and (5), we obtain $N_e/N_p \sim 20\eta_e$. In this case, the rest-frame width of the shell by the end of the shock evolution is $\lambda' \simeq 0.4(\Delta r/\Gamma_{\text{sh}}) \simeq 1.1 \times 10^{16}$ cm (see the Appendix in Moderski et al. 2004), and the density of the electrons and positrons is $n'_e = N_{e,\text{inj}}/(\pi R^2 \lambda')$, where $R = \theta_{\text{jet}} r$ is the cross-sectional

radius of the jet. Using these relations, one can estimate the energy flux carried by the protons,

$$L_p \simeq n'_p m_p c^3 \pi R^2 \Gamma_{\text{sh}}^2 \simeq n'_e \frac{N_p}{N_e} m_p c^3 \pi R^2 \Gamma_{\text{sh}}^2 \\ \sim 2.2 \times 10^{46} (1 - \eta_e) / \eta_e \text{ erg s}^{-1}. \quad (6)$$

This can be compared with the energy flux carried by the magnetic fields,

$$L_B \simeq \frac{B^2}{8\pi} c \pi R^2 \Gamma_{\text{sh}}^2 \simeq 6.3 \times 10^{45} \text{ erg s}^{-1}, \quad (7)$$

and by the electrons and positrons,

$$L_e \simeq n'_e \bar{\gamma}_{\text{inj}} m_e c^3 \pi R^2 \Gamma_{\text{sh}}^2 \simeq 5.6 \times 10^{45} \text{ erg s}^{-1}, \quad (8)$$

where L_e is estimated without taking into account radiative losses of the relativistic electrons and positrons and therefore is overestimated by a factor of ~ 4 .

4.4. Soft X-Ray Excess

Figure 11 shows in detail the optical–to–X-ray region of the SED. The hump on the left mimics excess emission from the dusty torus, as suggested by *IRAS* (Tanner et al. 1996), with a dust temperature of $kT \simeq 0.2$ eV and $L_{\text{dust}} \simeq 3.7 \times 10^{45}$ erg s $^{-1}$ (see also Table 6). The hump in the middle is our attempt to account for the blue bump, assuming an inner disk temperature of $kT \simeq 13$ eV and $L_{\text{disk}} \simeq 4 \times 10^{45}$ erg s $^{-1}$. We note here that the bolometric accretion luminosity is larger than this at least by a factor of 2, since more realistic models of accretion disks produce modified blackbody radiation, with extended high-energy tails and additional contribution from the more distant, cooler portions of the disk.

From the spectral fitting of the *Suzaku* data, we showed in § 3.1 and Table 4 that the soft X-ray excess may be represented either by a steep power law ($\Gamma_{\text{low}} \simeq 2.7$) or a blackbody-type emission of $kT \simeq 0.2$ keV. We investigate below whether such an excess can be produced by a bulk Comptonization of external

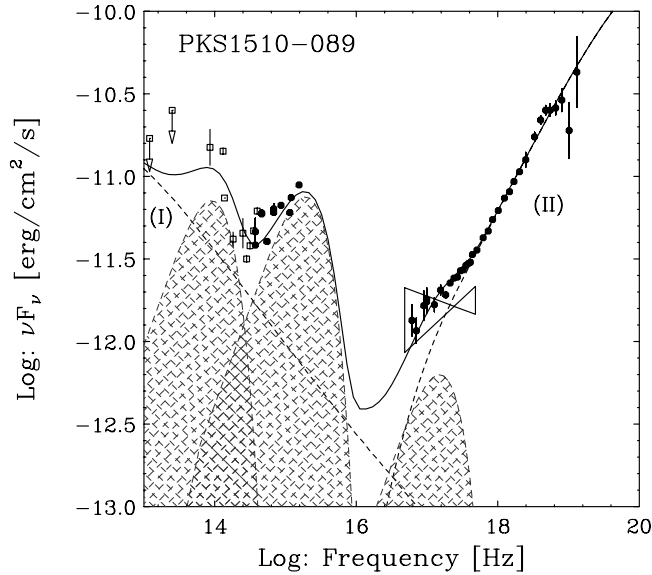


FIG. 11.—Close-up of the PKS 1510–089 SED model presented in Fig. 10 between the optical and the X-ray bands. Here three blackbody-type humps are added: the left hump mimics excess emission from the dusty torus, as suggested by *IRAS* (Tanner et al. 1996), whereas the middle hump mimics the blue bump expected for this source from combined *Swift* UVOT, REM, and Heidelberg data. The right hump shows the best-fit blackbody-type emission of $kT \simeq 0.2$ keV from the *Suzaku* fitting (Table 4). The dotted lines show (I) the synchrotron and (II) the EC components, respectively. The solid line shows the sum of all the model components. [See the electronic edition of the *Journal* for a color version of this figure.]

diffuse radiation by cold inhomogeneities or density enhancements prior to their collisions. At $r > r_{\text{BLR}}$, the density of the diffuse external UV radiation is very small, while the bulk Compton features from upscatterings of dust infrared radiation fall into the invisible extreme UV band. However, if acceleration of a jet has already occurred at $r \leq r_{\text{BLR}}$, upscattering of photons from the BLR should lead to formation of bulk Compton features, with peaks located around $\nu_{\text{BC},i} \sim \mathcal{D}_i \Gamma_i \nu_{\text{UV}} / (1+z)$ and luminosities of

$$L_{\text{BC},i} = \frac{4}{3} c \sigma_T u_{\text{BLR}} \Gamma_i^2 \mathcal{D}_i^4 N_{e,\text{obs},i}, \quad (9)$$

where $i = 1$ and 2, u_{BLR} is the energy density of the broad emission lines, \mathcal{D}_i is the Doppler factor, and $N_{e,\text{obs},i}$ is the number of electrons and positrons contributing to the bulk Compton radiation at a given instant (see Moderski et al. 2004). The above formulas apply to cylindrical jets and must be modified if used as approximations for conical jets. For the conical jets, the Doppler factor should be replaced by the “effective” Doppler factor, which for $\theta_{\text{obs}} \leq \theta_{\text{jet}}$ is $\mathcal{D}_i = \kappa \Gamma_i$, where $1 < \kappa < 2$. For our model parameters,

$$N_{e,\text{obs},1} \simeq \frac{N_{\text{inj}} r_{\text{BLR}}}{2 \lambda_0 \mathcal{D}_1}, \quad (10)$$

$$N_{e,\text{obs},2} \simeq \frac{N_{\text{inj}} r_{\text{BLR}} \Gamma_{\text{sh}}^2}{2 \lambda_0 \mathcal{D}_2 2\Gamma_2^2}, \quad (11)$$

where λ_0 is the proper width (longitudinal size) of the cold inhomogeneities (see Appendix A3 in Moderski et al. 2004); the factor $r_{\text{BLR}} / (\lambda_0 \mathcal{D}_i)$ is the fraction of particles observed at a given instant and takes into account that the source is observed as being stretched to the size $\lambda_0 \mathcal{D}_i$, which is larger than r_{BLR} ; and the extra factor in equation (11), $\Gamma_{\text{sh}}^2 / (2\Gamma_2^2)$, is the fraction of particles enclosed within the Doppler beam. With the above approximations and $\kappa = 1.5$, our model predicts the location of the bulk Compton features to be at ~ 1 and ~ 18 keV, with luminosities of $\sim 2 \times 10^{44}$

and 2×10^{46} erg s $^{-1}$, respectively. Comparing these luminosities with the luminosities of nonthermal radiation, we conclude that within the uncertainties regarding the details of the jet geometry and the model parameters, bulk Compton radiation produced by slower inhomogeneities is sufficiently luminous to be responsible for the soft X-ray excess observed by *Suzaku*, while the faster one can be tentatively identified with a small excess at ~ 18 keV seen in Figure 11.

4.5. On Alternative Models

The very hard X-ray spectrum measured by *Suzaku*, with $\Gamma_X < 1.5$, excludes models in which X-rays are produced by synchrotron radiation of the secondary ultrarelativistic population of electrons and positrons predicted by hadronic models, whereas the large luminosity ratio of the high- to low-energy components challenges the SSC models via enforcing magnetic fields much below the equipartition value (Moderski & Sikora 2007). No such constraints apply to EC models, provided that the jets are sufficiently relativistic. Furthermore, in the comoving frame of a jet moving with a Lorentz factor ≥ 6 , the energy density of seed photon fields is dominated by broad emission lines or infrared radiation of dust (depending on the distance of the source from the black hole), rather than by locally produced synchrotron radiation (Sikora et al. 1994). On the other hand, leptonic content of jets in the SSC models can be much smaller than that in the EC models, and therefore such models can easily avoid production of bulk Compton features, which in the context of EC models are predicted to be prominent (Moderski et al. 2004) but so far have not been observationally confirmed. However, that concern applies only to EC models with seed photons from the BLR. Production of similar high-energy spectra but at larger distances, where the external diffuse radiation field is dominated by near- to mid-infrared radiation, involves smaller leptonic content and therefore weaker bulk Compton features (M. Sikora et al. 2008, in preparation). Furthermore, the predicted bulk Compton features can be weaker in a scenario where the jet may still be in the acceleration phase while traversing the BLR (see Komissarov et al. 2007 and references therein).

If the latter is the case, the soft X-ray excess in PKS 1510–089 cannot originate from the bulk Compton process. A possible alternative origin of the observed soft X-ray excess may be then provided by the central regions of the accretion flow (Done & Nayakshin 2007), as seems to be the case in many nonblazar AGNs (Crummy et al. 2006 and references therein; see also Fig. 6 in Laor et al. 1997).

Yet another possibility for the origin of the observed soft X-ray excess would be due to a more significant contribution of the SSC component in a frequency range between the synchrotron and EC peaks, which would remain essentially invisible in the UV and hard X-ray bandpasses. In fact, we find that the collected data for PKS 1510–089 are consistent with another set of model parameters than those discussed previously (§§ 4.2–4.3), for which the soft X-ray excess is due to a combination of (1) the tail of the synchrotron component, (2) the EC emission and (3) the SSC emission falling in the soft X-ray band (Figs. 12 and 13; see also parameters of Model B in Table 6). Some discrepancies seen at 10^{17} – 10^{18} Hz are probably due to the mismatch of spectral slopes between the expected index of the SSC component ($\Gamma \simeq 2$) and the observed, steep excess emission ($kT \simeq 0.2$ keV or $\Gamma_{\text{low}} \simeq 2.7$). A steeper power-law contribution might naturally be provided just by the high-energy tail of the synchrotron emission, as often observed in low-frequency peaked blazars (e.g., Madejski et al. 1999; Tanihata et al. 2000; Tagliaferri et al. 2000). However, we note that extrapolation of this power law to lower frequencies

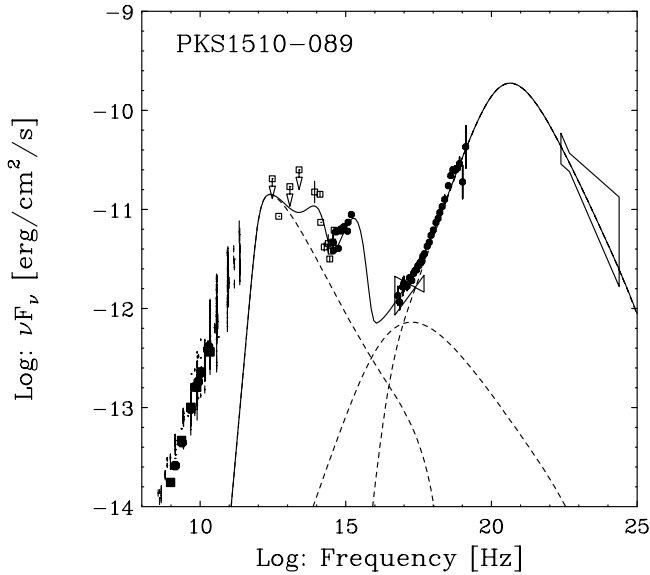


FIG. 12.—Same as Fig. 10, but with somewhat different input model parameters: $\gamma_{\min} = 1$, $\gamma_{\text{br}} = 150$, $\gamma_{\max} = 10^5$, $p = 1.35$, $q = 3.25$, $K_e = 1.7 \times 10^{47} \text{ s}^{-1}$, $\Gamma_{\text{jet}} = 20$, $\theta_{\text{jet}} = 0.02 \text{ rad}$, $\theta_{\text{obs}} = 0.05 \text{ rad}$, $r_{\text{sh}} = 10^{18} \text{ cm}$, $B = 0.86 \text{ G}$, $r_{\text{ext}} = 3.0 \times 10^{18} \text{ cm}$, $L_{\text{ext}} = 3.7 \times 10^{45} \text{ erg s}^{-1}$, and $h\nu_{\text{ext}} = 0.2 \text{ eV}$. [See the electronic edition of the Journal for a color version of this figure.]

overpredicts the observed IR/optical continuum by about an order of magnitude. Still, even if any of the above models proves to be more appropriate as a description of the soft excess, the results obtained in § 4.4 for the bulk Compton features should be considered as upper limits, which would then imply that the Lorentz factor of the jet is lower in the BLR region than at distances where the nonthermal radiation is produced.

5. CONCLUSIONS

We have presented a detailed analysis of the data for the powerful γ -ray-emitting quasar PKS 1510–089, obtained with the *Suzaku*, *Swift* XRT and UVOT, and ground-based optical (REM and Heidelberg) and radio (RATAN-600 and ATCA) telescopes. Observations were conducted in 2006 August as an intensive multiwavelength campaign lasting 3 weeks. An excellent broadband spectrum of the source was uniquely constructed, covering 10 decades in frequency, from 10^9 to 10^{19} Hz. Our major findings are as follows:

1. Deep *Suzaku* observations indicate moderate X-ray variability of PKS 1510–089 on the timescale of days, although differing in nature between the low-energy (0.4–1 keV) and high-energy (≥ 3 keV) bands.
2. The X-ray spectrum of PKS 1510–089 is well represented by an extremely hard power law (with a photon index of $\Gamma \simeq 1.2$) augmented by a blackbody-type component (with a temperature of $kT \simeq 0.2$ keV) that accounts for the excess emission below 1 keV.
3. *Swift* XRT observations reveal significant spectral evolution of the X-ray emission on the timescale of a week: the X-ray spectrum becomes harder as the source gets brighter.
4. Using the EC model, we found that the best fit of the broadband spectrum is obtained by assuming that nonthermal radiation is produced at $r > r_{\text{BLR}}$, where the external diffuse radiation field is dominated by IR radiation of hot dust.
5. The model predicts that the electron-to-proton ratio $N_e/N_p \sim 10$ and that the power of the jet is dominated by protons.
6. Prior to collisions and formation of shocks, density inhomogeneities interact with the BLR light and produce bulk Compton

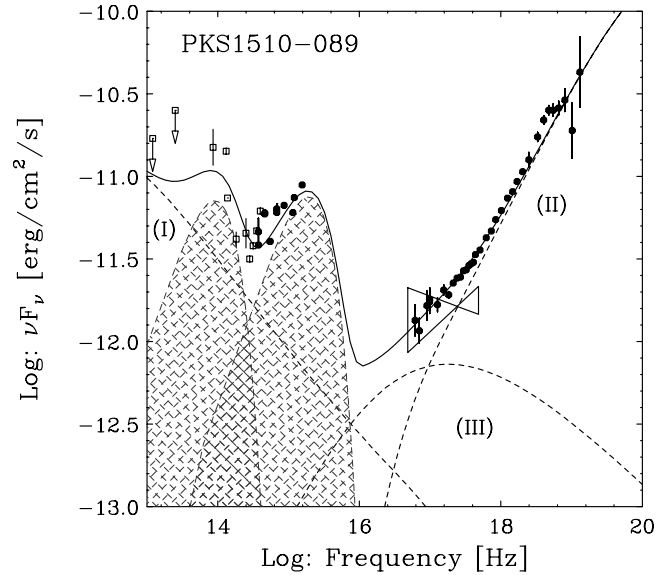


FIG. 13.—Close-up of the PKS 1510–089 SED model presented in Fig. 12 between the optical and the X-ray bands. The left hump mimics excess emission from the dusty torus, as suggested by *IRAS* (Tanner et al. 1996), whereas the right hump is that expected for this source from combined *Swift* UVOT, REM, and Heidelberg data. The dotted lines show the (I) synchrotron, (II) EC, and (III) SSC components. The solid line shows the sum of all the model components. [See the electronic edition of the Journal for a color version of this figure.]

features, which tentatively can be identified with the features observed in the *Suzaku* spectra: soft X-ray excess seen below ~ 1 keV, and another, marginally significant spectral feature at ~ 18 keV.

7. Alternatively, the soft X-ray excess can be explained as a contribution of the SSC component, or it can just be identified with the soft X-ray excess often observed in the nonblazar AGNs.

We are grateful to all the *Suzaku* members who helped us to analyze the data. We also thank all the *Swift* members (especially Neil Gehrels, who approved the target) for performing the ToO observations. We thank an anonymous referee for his or her helpful comments, which helped to clarify many of the issues presented in this paper. This work is sponsored at PSU by NASA contract NAS 5-00136. G. T. and D. I. thank the REM team for the support received during the observations. RATAN-600 observations were partly supported by the Russian Foundation for Basic Research (project 05-02-17377). The ATCA is part of the Australia Telescope, which is funded by the Commonwealth of Australia for operation as a National Facility managed by CSIRO. P. G. E. thanks Mark Wieringa for assistance with the ATCA observations. The authors made use of the database CATS (Verkhodanov et al. 1997) of the Special Astrophysical Observatory. This research has made use of the NASA/IPAC Extragalactic Database (NED), which is operated by the Jet Propulsion Laboratory, California Institute of Technology, under contract with the National Aeronautics and Space Administration. J. K. and N. K. acknowledge support by JSPS KAKENHI (19204017/14GS0211). G. M. and L. S. acknowledge support by the Department of Energy contract to SLAC, DE-AC3-76SF00515. M. S. and R. M. were partially supported by MEiN grant 1-P03D-00928. G. M. acknowledges support via NASA *Suzaku* grant NNX07AB05G. Y. Y. K. is a Research Fellow of the Alexander von Humboldt Foundation. L. S. was supported by MEiN through the research project 1-P03D-003-29 from 2005 to 2008.

REFERENCES

- Abbey, T., et al. 2006, in *The X-ray Universe*, ed. A. Wilson (ESA-SP 604; Noordwijk: ESA), 943
- Arnaud, K. A. 1996, in *ASP Conf. Ser. 101, Astronomical Data Analysis Software and Systems V*, ed. G. H. Jacoby & J. Barnes (San Francisco: ASP), 17
- Baars, J. W. M., Genzel, R., Pauliny-Toth, I. I. K., & Witzel, A. 1977, *A&A*, 61, 99
- Barthelmy, S. D., et al. 2005, *Space Sci. Rev.*, 120, 143
- Begelman, M. C., & Sikora, M. 1987, *ApJ*, 322, 650
- Bertin, E., & Arnouts, S. 1996, *A&AS*, 117, 393
- Burrows, D. N., et al. 2005, *Space Sci. Rev.*, 120, 165
- Burstein, D., & Heiles, C. 1982, *AJ*, 87, 1165
- Cappi, M., et al. 1997, *ApJ*, 478, 492
- Cardelli, J. A., Clayton, G. C., & Mathis, J. S. 1989, *ApJ*, 345, 245
- Celotti, A., Ghisellini, G., & Fabian, A. C. 2007, *MNRAS*, 375, 417
- Conconi, P., et al. 2004, *Proc. SPIE*, 5492, 1602
- Crummy, J., Fabian, A. C., Gallo, L., & Ross, R. R. 2006, *MNRAS*, 365, 1067
- Dermer, C. D., & Schlickeiser, R. 1993, *ApJ*, 416, 458
- Done, C., & Nayakshin, S. 2007, *MNRAS*, 377, L59
- Frater, R. H., Brooks, J. W., & Whiteoak, J. B. 1992, *J. Electrical Electron. Eng. Australia*, 12, 103
- Frontera, F., et al. 2007, *ApJ*, 666, 86
- Fukazawa, Y., et al. 2006, *Proc. SPIE*, 6266, 75
- Gambill, J. K., et al. 2003, *A&A*, 401, 505
- Gehrels, N., et al. 2004, *ApJ*, 611, 1005
- Georganopoulos, M., Kazanas, D., Perlman, E., & Stecker, F. 2005, *ApJ*, 625, 656
- Ghisellini, G., Celotti, A., Fossati, G., Maraschi, L., & Comastri, A. 1998, *MNRAS*, 301, 451
- Gruber, D. E., Matteson, J. L., Peterson, L. E., & Jung, G. V. 1999, *ApJ*, 520, 124
- Hartman, R. C., et al. 1999, *ApJS*, 123, 79
- Hill, J. E., et al. 2004, *Proc. SPIE*, 5165, 217
- Hirokuni, K. 2005, *ApJ*, 619, 73
- Homan, D. C., et al. 2001, *ApJ*, 549, 840
- Hoshino, A., Arons, J., Gallant, Y. A., & Langdon, A. B. 1992, *ApJ*, 390, 454
- Ishida, M., et al. 2006, *Suzaku Internal Rep. JX-ISAS-SUZAKU-MEMO-2006-40* (Sagamihara: ISAS), <http://www.astro.isas.jaxa.jp/suzaku/doc/suzakumemo/suzakumemo-2006-40.pdf>
- Jorstad, S. G., et al. 2005, *AJ*, 130, 1418
- Kataoka, J., et al. 1999, *ApJ*, 514, 138
- . 2001, *ApJ*, 560, 659
- . 2007, *PASJ*, 59, 279
- Koide, S., Meier, D., Shibata, K., & Kudoh, T. 2000, *ApJ*, 536, 668
- Kokubun, M., et al. 2007, *PASJ*, 59, S53
- Komissarov, S. S., Barkov, M. V., Vlahakis, N., & Königl, A. 2007, *MNRAS*, 380, 51
- Korolkov, D. V., & Pariiskii, I. N. 1979, *S&T*, 57, 324
- Kovalev, Y. Y., Nizhelsky, N. A., Kovalev, Yu. A., Berlin, A. B., Zhekanis, G. V., Mingaliev, M. G., & Bogdantsov, A. V. 1999, *A&AS*, 139, 545
- Koyama, K., et al. 2007, *PASJ*, 59, S23
- Kubo, H., Takahashi, T., Madejski, G., Tashiro, M., Makino, F., Inoue, S., & Takahara, F. 1998, *ApJ*, 504, 693
- Laor, A., Fiore, F., Elvis, M., Wilkes, B. J., & McDowell, J. C. 1997, *ApJ*, 477, 93
- Lawson, A. J., Turner, M. J. L., Williams, O. R., Stewart, G. C., & Saxton, R. D. 1992, *MNRAS*, 259, 743
- Lockman, F. J., & Savage, B. D. 1995, *ApJS*, 97, 1
- Lovelace, R. V. E., Ustyugova, G. V., & Koldoba, A. V. 1999, in *IAU Symp. 194, Active Galactic Nuclei and Related Phenomena*, ed. Y. Terzian, E. Khachikian, & D. Weedman (San Francisco: ASP), 208
- Madejski, G., et al. 1999, *ApJ*, 521, 145
- Makino, F., et al. 1989, *ApJ*, 347, L9
- Malkan, M. A., & Moore, R. L. 1986, *ApJ*, 300, 216
- Mirabel, I. F., & Rodríguez, L. F. 1999, *ARA&A*, 37, 409
- Mitsuda, K., et al. 1984, *PASJ*, 36, 741
- . 2007, *PASJ*, 59, S1
- Moderski, R., & Sikora, M. 2007, in *ASP Conf. Ser. 373, The Central Engine of Active Galactic Nuclei*, ed. L. C. Ho & J.-M. Wang (San Francisco: ASP), 207
- Moderski, R., Sikora, M., & Błażejowski, M. 2003, *A&A*, 406, 855
- Moderski, R., Sikora, M., Coppi, P. S., & Aharonian, F. 2005, *MNRAS*, 363, 954
- Moderski, R., Sikora, M., Madejski, G. M., & Kamae, T. 2004, *ApJ*, 611, 770
- Ott, M., Witzel, A., Quirrenbach, A., Krichbaum, T. P., Standke, K. J., Schalinski, C. J., & Hummel, C. A. 1994, *A&A*, 284, 331
- Page, K. L., Reeves, J. N., O'Brien, P. T., & Turner, M. J. L. 2005, *MNRAS*, 364, 195
- Pian, E., & Treves, A. 1993, *ApJ*, 416, 130
- Piran, T. 2000, *Phys. Rep.*, 333, 529
- Raiteri, C. M., Villata, M., Lanteri, L., Cavallone, M., & Sobrito, G. 1998, *A&AS*, 130, 495
- Romanova, M. M., & Lovelace, R. V. E. 1992, *A&A*, 262, 26
- Roming, P. W. A., et al. 2005, *Space Sci. Rev.*, 120, 95
- Sambruna, R., Tavecchio, F., Ghisellini, G., Donato, D., Holland, S. T., Markwardt, C. B., Tueller, J., & Mushotzky, R. F. 2007, *ApJ*, 669, 884
- Sambruna, R., et al. 2006, *ApJ*, 646, 23
- Sault, R. J., Teuben, P. J., & Wright, M. C. H. 1995, in *ASP Conf. Ser. 77, Astronomical Data Analysis Software and Systems IV*, ed. R. A. Shaw, H. E. Payne, & J. J. E. Hayes (San Francisco: ASP), 433
- Schlegel, D. J., Finkbeiner, D. P., & Davis, M. 1998, *ApJ*, 500, 525
- Serlemitsos, P. J., et al. 2007, *PASJ*, 59, S9
- Siebert, J., et al. 1996, *MNRAS*, 279, 1331
- Sikora, M., Begelman, M. C., Madejski, G. M., & Lasota, J.-P. 2005, *ApJ*, 625, 72
- Sikora, M., Begelman, M. C., & Rees, M. J. 1994, *ApJ*, 421, 153
- Sikora, M., Błażejowski, M., Moderski, R., & Madejski, G. M. 2002, *ApJ*, 577, 78
- Sikora, M., & Madejski, G. M. 2000, *ApJ*, 534, 109
- Sikora, M., Madejski, G., Moderski, R., & Poutanen, J. 1997, *ApJ*, 484, 108
- Singh, K. P., Shrader, C. R., & George, I. M. 1997, *ApJ*, 491, 515
- Sokolov, A., & Marscher, A. P. 2005, *ApJ*, 629, 52
- Spada, M., Panaitescu, A., & Meszaros, P. 2000, *ApJ*, 537, 824
- Stawarz, Ł., Cheung, C. C., Harris, D. E., & Ostrowski, M. 2007, *ApJ*, 662, 213
- Stetson, P. B. 1987, *PASP*, 99, 191
- Tagliaferri, G., et al. 2000, *A&A*, 354, 431
- Takahashi, T., et al. 2007, *PASJ*, 59, S35
- Tanihata, C., Takahashi, T., Kataoka, J., & Madejski, G. M. 2003, *ApJ*, 584, 153
- Tanihata, C., et al. 2000, *ApJ*, 543, 124
- Tanner, A. M., Bechtold, J., Walker, C. E., Black, J. H., & Cutri, R. M. 1996, *AJ*, 112, 62
- Tavecchio, F., Maraschi, L., Ghisellini, G., Kataoka, J., Foschini, L., Sambruna, R. M., & Tagliaferri, G. 2007, *ApJ*, 665, 980
- Tavecchio, F., et al. 2000, *ApJ*, 543, 535
- Tingay, S. J., Jauncey, D. L., King, E. A., Tzioumis, A. K., Lovell, J. E. J., & Edwards, P. G. 2003, *PASJ*, 55, 351
- Tosti, G., Pascolini, S., & Fiorucci, M. 1996, *PASP*, 108, 706
- Tosti, G., et al. 2004, *Proc. SPIE*, 5492, 689
- Uchiyama, Y., et al. 2005, *ApJ*, 631, L113
- Urry, C. M., & Padovani, P. 1995, *PASP*, 107, 803
- Verkhodanov, O. V., Trushkin, S. A., Andermach, H., & Chernenkov, V. N. 1997, in *ASP Conf. Ser. 125, Astronomical Data Analysis Software and Systems VI*, ed. G. Hunt & H. E. Payne (San Francisco: ASP), 322
- Villata, M., et al. 1997, *A&AS*, 121, 119
- Wardle, J. F. C., Homan, D. C., Cheung, C. C., & Roberts, D. H. 2005, in *ASP Conf. Ser. 340, Future Directions in High Resolution Astronomy*, ed. J. D. Romney & M. J. Reid (San Francisco: ASP), 67
- Wardle, J. F. C., Homan, D. C., Ojha, R., & Roberts, D. H. 1998, *Nature*, 395, 457
- Williams, O. R., et al. 1992, *ApJ*, 389, 157
- Zdziarski, A. A., Poutanen, J., & Johnson, W. N. 2000, *ApJ*, 542, 703
- Zerbi, F. M., et al. 2004, *Proc. SPIE*, 5492, 1590